An experimental apparatus for diffraction-limited soft x-ray nano-focusing

Daniel J. Merthe,[1] Kenneth A. Goldberg,[2] Valeriy V. Yashchuk,[1] Sheng Yuan,[1] Wayne R. McKinney,[1] Richard Celestre,[1] Iacopo Mochi,[2] James Macdougall,[2] Gregory Y. Morrison,[3] Senajith B. Rakawa,[3] Erik Anderson,[3] Brian V. Smith,[3] Edward E. Domning,[3] Tony Warwick,[1] Howard Padmore[1]

[1]Advanced Light Source, Lawrence Berkeley National Laboratory, Berkeley, CA 94720
[2]Center for X-Ray Optics, Lawrence Berkeley National Laboratory, Berkeley, CA, 94270
[3]Engineering Division, Lawrence Berkeley National Laboratory, Berkeley, CA, 94270

ABSTRACT

Realizing the experimental potential of high-brightness, next generation synchrotron and free-electron laser light sources requires the development of reflecting x-ray optics capable of wavefront preservation and high-resolution nano-focusing. At the Advanced Light Source (ALS) beamline 5.3.1, we are developing broadly applicable, high-accuracy, *in situ,* at-wavelength wavefront measurement techniques to surpass 100-nrad slope measurement accuracy for diffraction-limited Kirkpatrick-Baez (KB) mirrors.

The at-wavelength methodology we are developing relies on a series of wavefront-sensing tests with increasing accuracy and sensitivity, including scanning-slit Hartmann tests, grating-based lateral shearing interferometry, and quantitative knife-edge testing. We describe the original experimental techniques and alignment methodology that have enabled us to optimally set a bendable KB mirror to achieve a focused, FWHM spot size of 150 nm, with 1 nm (1.24 keV) photons at 3.7 mrad numerical aperture. The predictions of wavefront measurement are confirmed by the knife-edge testing.

The side-profiled elliptically bent mirror used in these one-dimensional focusing experiments was originally designed for a much different glancing angle and conjugate distances. Visible-light long-trace profilometry was used to pre-align the mirror before installation at the beamline. This work demonstrates that high-accuracy, at-wavelength wavefront-slope feedback can be used to optimize the pitch, roll, and mirror-bending forces *in situ*, using procedures that are deterministic and repeatable.

Keywords: metrology of x-ray optics, synchrotron radiation, nano-focusing, shearing interferometry, Hartman test, knife edge measurement.

1. INTRODUCTION

With the rapid advent and advance of nanotechnology in recent times, the nano-scale world has experienced an increasingly bright spotlight. Suddenly, the potential realization of engineered nanomaterials, such as self-organized nanostructures, correlated materials and microcrystallines, has prompted a burgeoning scientific mission to observe and understand the physics of the very small. However, bridging the current chasm between ambition and reality in this respect requires an apposite extension of technology. Such endeavors towards improving the resolution and quality of beamline optics at the Advanced Light Source (ALS) confront severe challenges.

Despite great advances in optics fabrication and *ex situ* (visible-light) metrology, the experimental resolution and spot size of typical x-ray beamlines at synchrotron radiation facilities are often limited by misalignment, mechanical actuation, position drift, vibration and the gradual degradation or contamination of optics exposed to intense beams of light. Therefore, in order to take full advantage of current high-brightness synchrotron light sources, such as Lawrence

Advances in X-Ray/EUV Optics and Components VI, edited by Christian Morawe, Ali M. Khounsary, Shunji Goto,
Proc. of SPIE Vol. 8139, 813907 · © 2011 SPIE · CCC code: 0277-786X/11/$18
doi: 10.1117/12.894116

Berkeley National Laboratory's Advanced Light Source (ALS), and so-called *next generation* sources, practical methods must be developed to provide *in-situ*, at-wavelength optical metrology and feedback for the optimization of x-ray wavefront quality leading to the reliable creation of nano-focused beams.

The principal challenge in conducting high precision, at-wavelength optical metrology is maintaining a stable experimental system amid the noisy environment of a synchrotron beamline. To this end, we developed an apparatus designed to separate a soft x-ray experimental metrology endstation from its beamline source. Primarily, this involved isolation of the test chamber from the myriad vibration sources (pumps in particular), temperature stabilization, and the creation of an internal, shared alignment system for all of the optical elements. The methods used to achieve these objectives are discussed in Section 2.

Furthermore in this study, which is an extension of previous work[1,2], we describe a comprehensive experimental method that enables the *in situ*, at-wavelength alignment and bending optimization of a single, elliptically-focusing Kirkpatrick-Baez (KB) mirror, resulting in mirror slope errors of 240 nrad, and a spot size that repeatedly reaches the diffraction limit of ~150 nm. Using a single, vertically focusing KB mirror permits a straightforward demonstration of the methodology. The mirror is configured with a source demagnification ratio of 13.0 and an image-side numerical aperture (NA) close to 3.7 mrad. All tests were conducted using 1-nm-wavelength illumination, provided by a tunable, double-multilayer monochromator, with a thin aluminum foil to block longer-wavelength light. Nano-focusing is accomplished by performing a series of interferometric and non-interferometric tests, including lateral shearing interferometry[3] for wavefront slope retrieval. Ultimately, the results of the optimization process, elaborated in Section 4, are verified by a Foucault knife-edge analysis. By employing quantitative wavefront or slope feedback from the procedures discussed herein, we believe that many adjustable x-ray optical systems could be optimized to achieve the highest possible wavefront quality, including focusing at or near the diffraction limit.

Ultimately, we also seek to demonstrate the correspondence between *in situ* (at-wavelength) and *ex situ* (visible-light) metrologies. For this reason, another important facet of this work is the comparison of results obtained at the beamline with those obtained in the ALS Optical Metrology Laboratory (OML). Specifically, the tests conducted in the OML measure and improve the slope, or *slope errors*, of glancing-incidence beamline optics. Section 4 presents the method of 1D lateral shearing interferometry which measures the wavefront slope (at some point along the beam), and from which the slope error across the mirror can be computed. Section 5 also describes the transformation between wavefront slope error and mirror slope error.

2. A STABILIZED AND CONTROLLED EXPERIMENT

In creating the experimental system, our primary goal was to ensure stability with respect to thermal variations and mechanical vibrations. This section describes the key components of the design, and our measurement of the residual vibration magnitude.

2.1 Structural isolation of internal components

The experimental apparatus developed for the optical metrology beamline 5.3.1 at the ALS is illustrated in Fig. 1. In order to create the most stable environment, we designed all of the optical components (the single KB mirror and both conjugate planes) to be on a single breadboard, isolated from the external environment of the beamline endstation. The internal optical breadboard is housed inside a $2.0 \times 0.5 \times 0.5$ m^3 vacuum chamber. All optical components are placed in-line on a single Thorlabs™ XT95 optical rail (mounted on the breadboard) to facilitate mutual alignment and positioning of the components. The breadboard is held free from the vacuum chamber walls, coupled through flexible bellows to an exterior alignment rail that is mounted on a large optical bench via a six-strut Stewart Platform mount[4]. Because much of the electromechanical equipment (pumps, equipment controllers, etc.) is attached to or resting on the vacuum chamber, decoupling the internal breadboard from the vacuum chamber walls alleviates most vibration issues. The external optical bench also supports the vacuum chamber. To record the projected image of the pupil, a charged coupled device (CCD) camera is connected to the end of a 1.5-meter-long tube attached to the vacuum chamber.

For mechanical stability, the internal, aluminum breadboard is attached to the exterior 80/20 rails by three stainless steel cross-bars. Symmetric, trapezoidal, aluminum expansion joints between the breadboard and the cross-bars (Fig. 1B, inset) maintain the relative position of the optical components in the beam in the presence of temperature changes, despite the different thermal expansion coefficients. A finite-element analysis of the internal breadboard/support-bar/rail system indicates a maximum deformation due to gravity of 130 μm.

Another important design feature of this system is the kinematic ball-and-groove mounts that hold the image plane and object plane optical elements (i.e. pinholes, slits, gratings, knife-edge, etc.) onto their stages with magnetic coupling. These components are occasionally removed, adjusted, and remounted into the vacuum chamber. To facilitate this and to preserve their alignment in the beam, a kinematic alignment strategy allows the parts to mechanically *snap* into their home position, where magnets hold them in place.

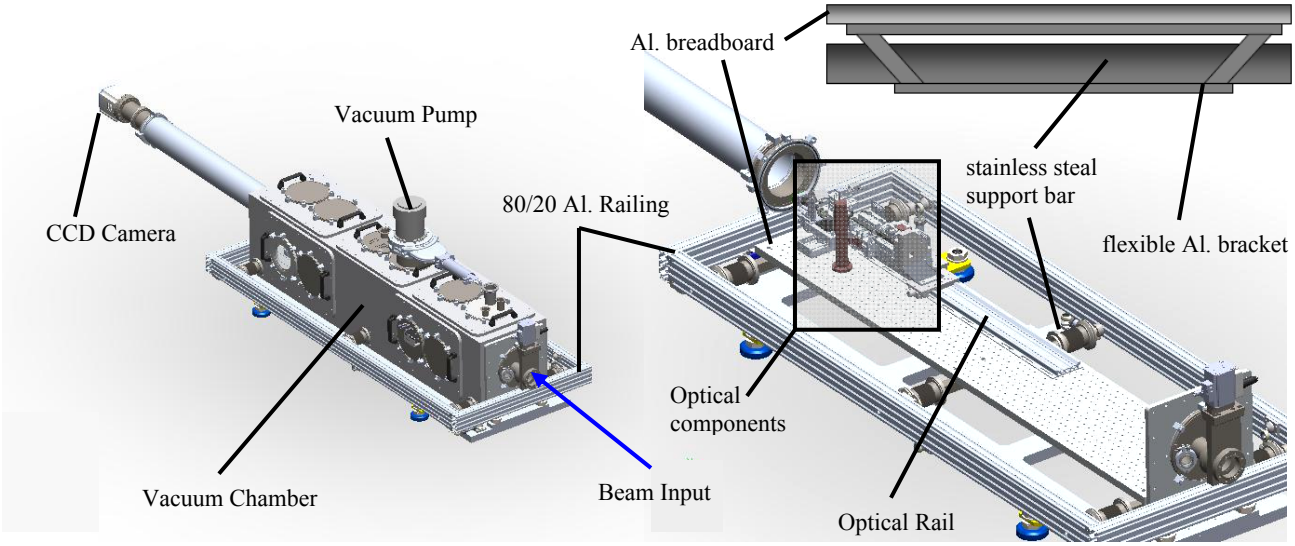

Figure 1. Beamline endstation chamber design. (Left) The experiment is housed inside an aluminum vacuum chamber, with an attached charged coupled device (CCD) camera. (Right) The internal aluminum breadboard is connected through flexible bellows to the exterior 80/20 alignment railing by three stainless steal support bars. A trapezoidal expansion joint (inset) connects the breadboard to the railing, and maintains the relative beam position in the presence of temperature variation.

2.2 Vibration assessment of internal optics

Even with the high degree of isolation, some residual vibration remains. Using a combination of knife-edge measurements with a downstream photodiode, we measured the vertical oscillation of the x-ray beam with respect the optical elements, and the beam-power fluctuations that originate from sources upstream of the chamber. A narrow, 1-μm slit in the object plane produces a cylindrical wavefront that fills the pupil of the single KB mirror. An image of the slit is formed in the focal plane. Random, oscillatory motion of the focused x-ray beam ultimately increases the measured spot size; while temporal variations in the light intensity can degrade of the measurement of the beam profile.

To separate the beam position and power variations experimentally, we first create a simple, statistical model of the beam. Over the course of many experiments it has become apparent that the shape of the beam is roughly Gaussian in the focusing direction. Therefore, when an opaque knife-edge is scanned vertically across the beam to a position y relative to the beam, the measured power P of the beam immediately downstream of the knife-edge is given by

$$P(y, P_0, \varepsilon) = \frac{P_0}{2}\left(1 + Erf\left(\frac{y}{w\sqrt{2}}\right)\right) + \varepsilon, \tag{1}$$

where ε is electronic noise (i.e. likely not from the optical system, because it has no effect on the geometry of the beam), P_0 is the power level of the beam, and w is the vertical-direction standard deviation of the beam profile and is proportional to the full-width at half maximum (FWHM). The origin of the y-axis is chosen to coincide with the average center of the beam. If the parameters ε, P_0 and the variable y vary independently and in small proportions, then the variance of the power $\sigma^2[P]$ with y centered at $\langle y \rangle$ (angle brackets indicate the expected value) is approximately

$$\sigma^2[P] \approx \left(\frac{1}{2} + \frac{1}{2} Erf\left(\frac{\langle y \rangle}{w\sqrt{2}}\right)\right)^2 \sigma^2[P_0] + \frac{\langle P_0 \rangle^2}{2\pi w^2} \exp\left[-\langle y \rangle^2 \Big/ w^2\right] \sigma^2[y] + \sigma^2[\varepsilon]. \quad (2)$$

Now we consider three measurement conditions. First we consider a power measurement P_1 over time, in a configuration where the knife completely blocks the beam $\left(\langle y \rangle = -\infty\right)$, then no light is observed and no beam motion is seen. Here all of the measured variation comes from the electronic noise alone: $\sigma^2[P_1] = \sigma^2[\varepsilon]$. In a second power measurement P_2, the knife-edge is retracted to allow the full beam to pass $\left(\langle y \rangle = \infty\right)$; the observed power variance is the combination of the beam fluctuations and electronic noise: $\sigma^2[P_2] = \sigma^2[P_0] + \sigma^2[\varepsilon]$. Finally, a third measurement P_3 places the knife-edge at the center of the beam, where ½ of the power is blocked, $\left(\langle y \rangle = 0\right)$. In this case, the observed power variation comes from all three sources, which add in quadrature: $\sigma^2[P_3] = \sigma^2[P_0]/4 + \langle P_0 \rangle^2 \sigma^2[y]/2\pi w^2 + \sigma^2[\varepsilon]$. Combining these three measurements, the variance of ε, P_0 and y can each be isolated in turn.

$$\sigma[\varepsilon] = \sigma[P_1]. \quad (3a)$$

$$\sigma[P_0] = \sqrt{\sigma^2[P_2] - \sigma^2[P_1]}. \quad (3b)$$

$$\sigma[y] = w\sqrt{2\pi}\sqrt{\left(\sigma^2[P_3] - 0.75\sigma^2[P_1] - 0.25\sigma^2[P_2]\right)/\langle P_2 \rangle}. \quad (3c)$$

The expected value $\langle P_0 \rangle$ is replaced by the mean power of the second measurement $\langle P_2 \rangle$, which serves as the best estimate. Notice that the coefficient $w\sqrt{2\pi}$ in Eq. (3c) is roughly equal to the FWHM of the Gaussian beam, such that the standard deviation of beam position is directly comparable to this width. Then the term with the radical in Eq. (3c) is the RMS variation of the beam position (relative to the knife-edge) as a fraction of the beam width. In other words, this is the amount of beam width dilation seen by the CCD, relative the actual width of the beam.

The three power measurements described above were carried out using a knife-edge in the focal plane, and a single-element photodiode a few cm downstream. Measurements were made using a sampling rate of 1.67 kHz. These measurements were taken after the optimization of the optical system (discussed below), with the measured beam width w close to 150 nm. Both the oscillation of the beam with respect to the chamber and the power fluctuations exhibit common low-level broadband noise characteristics, along with larger amplitude oscillations in specific frequencies below 200 Hz. This indicates a shared response to the mechanical vibrations of the facility. Separately, the electronic noise component contains a series of harmonic frequencies with a 35-Hz fundamental.

Overall, we found that the estimated root mean square variation of the beam position y is 3% of the FWHM or ~5 nm. The root mean square power variation $\sigma[P_0]$ as a percent of $\langle P_0 \rangle$ was approximately 2% and that of the electronic noise error was 3%. This test was conducted while the ALS was in a special timing mode called *two-bunch mode,* during which the beam power is an order of magnitude lower than usual. Subsequent measurements made with lower sampling frequencies (100 Hz) and the ALS in normal operating mode yielded somewhat different results: $\sigma[y]$ =10 nm, and $\sigma[\varepsilon]$ = 2%, and $\sigma[P_0]$ = 15% of $\langle P_0 \rangle$. This latter value for power level fluctuations shows that while the internal optical components are well isolated from external vibrations (corresponding to low vales of $\sigma[y]$) the vibrations of the beamline can still affect experiments through intensity fluctuations. We note that this error has little effect on lateral shearing interferometry and scanning-slit measurements in which the interferograms or projected slit patterns are effectively time-averaged and are analyzed independently. This is discussed in Section 4.

Prior to installation on the beamline, the vibration response of the mirror-bending mechanism was evaluated using a vibrometer. The mirror vibration mode related to the mechanism for (grazing incidence) pitch-angle adjustment peaks is at 84.5 Hz with Q-factor of about 50. The mode associated with the mechanism for alignment of the mirror roll angle has frequency of about 230 Hz and rather small Q-factor of about 10. Due to the mirror-holder design, the vibration of the roll-adjustment mechanism can contribute to the instability of the mirror pitch angle. We also found a vibration mode of the bender mechanism that can potentially lead to an oscillation of the mirror shape. The frequency of this mode is 157.2 Hz, with a Q-factor of about 15.

We have also performed similar vibrometer measurements searching for the vibration modes of the aluminum breadboard inside the end-station vacuum chamber. We found a strong roll-angle breadboard vibration mode at 85 Hz, and Q-factor is about 30.

Therefore, among the known vibration modes of the mirror assembly, the pitch mode at 84.5 Hz is potentially the most troublesome: it could directly affect the focus spot position; it has a relatively large Q-factor; and the frequency of the mode is very close to that of the breadboard vibration mode. Fortunately, resonance at this frequency was not detected in the *in situ* knife-edge vibration tests described above.

3. AT-WAVELENGTH METROLOGY TOOLS AND TESTS

The various at-wavelength metrology tests share a compact set of entrance apertures and nanofabricated patterns on two transmission membranes located in the conjugate planes. The optical components used in the at-wavelength metrology tests are illustrated in Fig. 3. Note that all measurements were performed at 1-nm wavelength.

A cylindrical reference wavefront, created by a horizontal slit in the object plane, illuminates the test mirror. The slit is selected from an array of electron-beam-fabricated slits that are 200-μm long and have opening widths between 0.66 and 6 μm. The absorber is a 1-μm-thick Au membrane, patterned on a 100-nm-thick silicon-nitride membrane. The slit is placed at the intermediate focus of the beamline and serves as a virtual source for the experiment[2,5], over-filling the mirror's aperture. The same array contains pinholes of various sizes, for spherical wave illumination of future two-dimensional focusing experiments. Reference 1 contains more details about the optical configuration upstream of the object array.

The elliptical KB test mirror was developed at the OML[6,7] specifically for metrology experimentation. Its center is placed 1656 mm downstream of the entrance slit. The focal distance is estimated to be 120 mm from the mirror's center. For elliptically focusing mirrors, these conjugate distances are commonly referred to as r and r', respectively (see Refs. 8 and 9). The shape of the mirror is adjusted *in situ* by two bending couples attached to the upstream and downstream ends and operated using the bendable mirror adjustment methods described in Refs. [8-10]. By design, the central glancing angle of incidence on the mirror is $\theta = 8$ mrad. Using the length of the beam projection on the CCD and the known distance from focus, we measured a maximum image-side NA value of 3.7 mrad for the test mirror.

Four kinds of metrology were used to quantify the performance of the KB mirror. These tests are referred to as the upstream scanning slit, the Foucault knife-edge, the downstream scanning slit, and lateral shearing interferometry. They are described in some detail in Ref. [2], and briefly here, below. The optical structures used in these tests (gratings, slit, knfe-edge) share a single, 2×2 mm nanostructure also fabricated in an Au absorber on a silicon-nitride window. The nanostructure is mounted perpendicular to the chief ray, 8 mrad from vertical.

It is important to note and to account for the non-linear mapping of points on the mirror surface to projected-light positions on the downstream CCD camera, arising from the curved shape of the mirror. The incident ray fan is distributed non-linearly on the surface of the mirror, with the rays bunching up on the downstream end. Similarly, rays from uniformly sampled points on the mirror surface are mapped to non-uniformly distributed positions on the CCD. Thus translating measurements from one coordinate system to another (e.g. from the CCD to the mirror surface) requires a coordinate transformation. We rely on a Zemax™ model to provide the interpolation empirically.

3.1 Upstream scanning-slit test

The upstream scanning slit test[11] (Fig. 3A) is conducted using the JJ X-Ray™ slit system with a narrow opening (below 100 μm) to isolate each part of the mirror in a series of discrete steps. By observing the motion of the beam position in or near the focal plane as the slit is moved (using a YAG and in-vacuum CCD microscope), we can identify wavefront slope errors from each part of the mirror. If the alignment were perfect, all parts of the mirror would focus light to the same position and the measured beam would not move with the slit position.

3.2 Downstream scanning slit test

A downstream scanning slit test is conceptually similar to the upstream scanning slit test, but behaves more like a Hartmann test with a scanning aperture rather than a static grid. It uses a 10-μm-wide slit several mm beyond the focus, and the beam is projected on the downstream CCD (Fig. 3C). Like a Hartmann test,[11-13] the positions (i.e. centroids) of the projected beam, as a function of slit position, reveal the slope of the wavefront point-by-point.

The upstream scanning-slit test, with the CCD positioned in focus, has the advantage that the results are unambiguous. Whether or not all points in the mirror focus to the same point is readily apparent and not subject to misinterpretation. Its disadvantage is a higher slope measurement uncertainty from the short distance between the mirror and focus (120 mm) and from the blur of the visible-light image on the YAG (several μm in our case). The long distance to the CCD (~1.5 m), and the direct soft x-ray detection provides the downstream scanning-slit technique with improved slope measurement precision. In both tests, the transformation between the slit position and the position where the selected rays reflected from the mirror surface requires a non-linear mapping. However, since the downstream test performs its measurement on the same side of the mirror as the focus, the measurements correspond directly to the wavefront slope errors in the focusing beam.

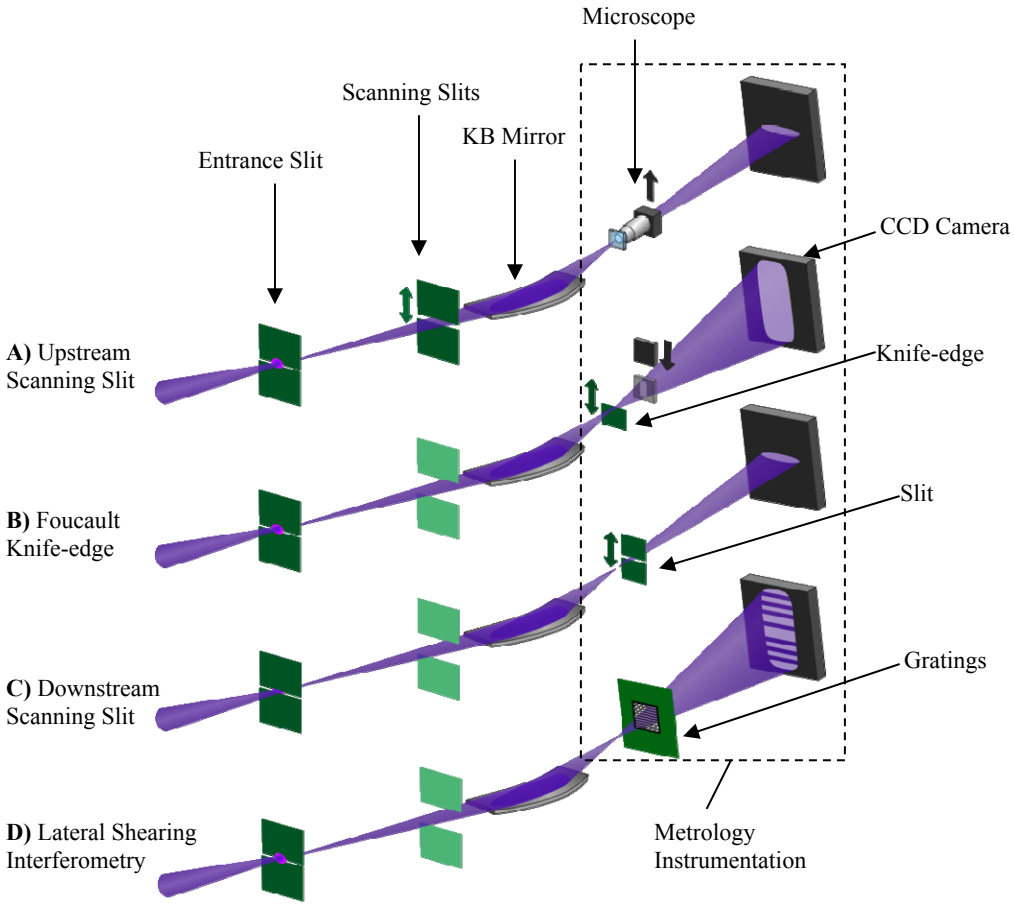

Figure 2. Optical system layout for the four metrology tests.

3.3 Two knife-edge tests

In principle, there are *two* knife-edge tests; both utilize a moving, nanofabricated, opaque "knife" edge near focus. The simple version translates a knife in steps, through the beam's focused spot and records the transmitted intensity on a single-element photodiode placed downstream of the knife, or onto a CCD camera where the signal can be summed. This test enables unambiguous measurement of the beam size, as shown in Figs. 3B and Refs [14-16]. The second version of the knife-edge tests records the projected beam on the downstream CCD camera, as the knife transitions through focus. Recordings of the diffracted shadow of the knife-edge are called *Foucaultgrams*. Within the measured pupil, each pixel in the detector corresponds to a unique point in the wavefront and a position on the mirror's surface. By observing the moving shadow on the CCD, and recording the knife position where the beam intensity transitions through 25% if its peak value (at each pixel), we can create a wavefront slope-map point by point. (For coherent illumination, the 25%

intensity point shows where the beam is cut in half). Both methods are sensitive to fluctuations in the beam illumination during the data collection, which can be lengthy (i.e. minutes). We refer to the second version as the *quantitative* knife-edge test.

3.4 Lateral shearing interferometry

In shearing interferometry, displaced copies of the test wavefront are compared interferometrically, and small differences are revealed in the resultant fringe pattern. A linear, binary, transmission-grating structure, with 1:1 line-to-space ratio is positioned downstream of the focus to create multiple beam interference at the CCD detector (Fig. 3D). Several gratings are available on the same nanofabricated membrane that contains the scanning slit and knife-edge used in the tests described above. We choose relatively coarse grating pitch values (4, 5, and 6 μm) in order to achieve a large overlap among the interfering beams. To produce high fringe contrast, the grating is placed with the focus close to the first Talbot plane distance,[3,17] $Z_g \approx d^2/\lambda$ (= 16, 25, or 36 mm, respectively for the three gratings).

4. AT-WAVELENGTH OPTIMIZATION OF THE OPTICAL SYSTEM

In general at-wavelength measurement and optimization requires that the mirror be pre-aligned, and then bent into a configuration close to its final, desired state. Each test has a different capture range, and ability to tolerate large aberrations, with the scanning slit tests likely having the largest range. As described in Ref. 1, the mirror pre-alignment process begins in the ALS OML with the setting of the KB mirror using slope measurements from the ALS Second Generation Upgraded Long Trace Profiler (LTP-II++)[18-20] and a variation of regression analysis,[9,10] referred to as the *Method of Characteristic Functions* (MCF) in this work. MCF is described in Section 4.1. Following visible-light shape optimization, the KB mirror is installed in the beamline endstation for at-wavelength characterization and further optimization.

Initial at-wavelength alignment consists of tilting the mirror (i.e. changing the glancing angle of incidence) and using the YAG/microscope to observe the beam width in the assumed focal plane. Tilting changes the mirror's glancing angle of incidence, and hence the focal length. The optimal tilt can be identified in a few iterations, by observing changes in the beam's size, and selecting the minimum value.

The second step in the alignment is the fine adjustment of the mirror tilt and the focal plane position, using the upstream scanning slit method to characterize the slope errors. In our experience, this fine adjustment in conjunction with MCF was effective at bringing the beam spot size down below 1 μm within a two or three iterations. Here, the two input parameters for the MCF optimization are the tilt angle, and the longitudinal (focal) position of the YAG. The downstream scanning slit test is also being evaluated for use as an alternative to the upstream scanning slit test.

Once the best tilt and focal plane have been identified coarsely, lateral shearing interferometry, guided by the MCF, is used as rapid, quantitative feedback to adjust the bending couples and minimize wavefront aberrations up to fourth order. Finally, the resulting "optimum" configuration is verified using the Foucault knife-edge test.

4.1 Method of characteristic functions for general optimization

Optimization by the method of characteristic functions is an application of linear regression to a system with some merit function $G(x)$, e.g. slope error at x.[9,10] We assume that for small adjustments, this function is linear in some free parameters $\{\alpha_j\}$, such that a measurement of G at point x_i is described by

$$G(x_i;\alpha_j) = G^{(0)}(x_i) + \sum_i \alpha_j f_j(x_i) + \varepsilon_i . \tag{4}$$

where $G^{(0)}(x_i)$ is the ideal merit function, and the set of functions $f_j(x)$ are called the *characteristic functions* of the system. The ε_i term is the error of the measurement (with respect to the model). The characteristic functions are measured by observing the relative changes in the system state, $G(x)$, induced by small changes in the free parameters.

$$f_j(x_i) = \frac{\partial G}{\partial \alpha_j}(x_i) \approx \frac{G(x_i;\alpha_j + \Delta\alpha_j) - G(x_i;\alpha_j)}{\Delta\alpha_j} . \tag{5}$$

Here $\Delta\alpha_j$ represents a small change in the parameter α_j. Inserting the measured characteristic functions into Eq. (4), the optimization problem reduces to linear regression analysis, wherein the variance of ε_i is minimized with respect to the

parameters α_j. The solution set $\{\alpha^*_j\}$ is interpreted as the recommended change in the free parameters $\{\alpha_j\}$ to bring the system as close to $G^{(0)}(x_i)$ as possible.

4.2 Initial at-wavelength optimization of mirror tilt and focal length

The MCF is used routinely in the OML to shape bendable mirrors.[9,10] Once the KB test mirror for this experiment is shaped accordingly in the OML and placed at the beamline, the mirror must go through an initial angular alignment step, which is described in more detail in the identical procedure of Ref. 1. The focusing ability of the mirror is highly sensitive to the incidence angle of the x-ray beam on the mirror surface. Hence, before the mirror can be further shaped at the beamline, the optimum incidence angle (about ~8 mrad) must be determined. To find this optimum angle of reflection, we vary, from an initial state, both the tilt of the mirror (KB_{tilt}) and the observation plane position (OPP) about the focus, where the beam position is observed with a YAG crystal microscope downstream of the mirror (shown in Fig. 3A), and then MCF is applied to find the optimum settings of these parameters. We must vary the OPP, because as the tilt of the mirror changes so does the effective focal plane. Hence, we need to simultaneously find both the optimal mirror tilt and its corresponding effective focal plane.

Using the visible-light microscope image of the YAG, the observed size of the beam was never less than 6 μm, due to blooming and focusing errors in the microscope. This is much broader than the soft x-ray beam. Nonetheless, the method can be highly sensitive sub-half-micron to the motion of the beam centroid that tracks the beam position variations we seek to measure.

The figure of merit in this calculation is the RMS variation in the vertical position y of the beam centroid as a function of the vertical position x of the upstream scanning slit. If the mirror is perfectly focused and the OPP is in the effective focal plane, then the beam incident on the camera will be stationary. This defines the ideal figure of merit, $y^{(0)}(x) = constant$. Since the vertical beam position is arbitrary, we include this constant in the linear regression analysis, eliminating its influence on the variance of ε_i.

The left graph in Fig. 3 illustrates the changes in the measured $y(x)$, as the mirror is tilted by ΔKB_{tilt} = +460 μrad (positive when the mirror becomes more parallel to the beam), and as ΔOPP = +1 mm from the initial state (solid line). The graph on the right shows the measured characteristic functions, resulting from these changes.

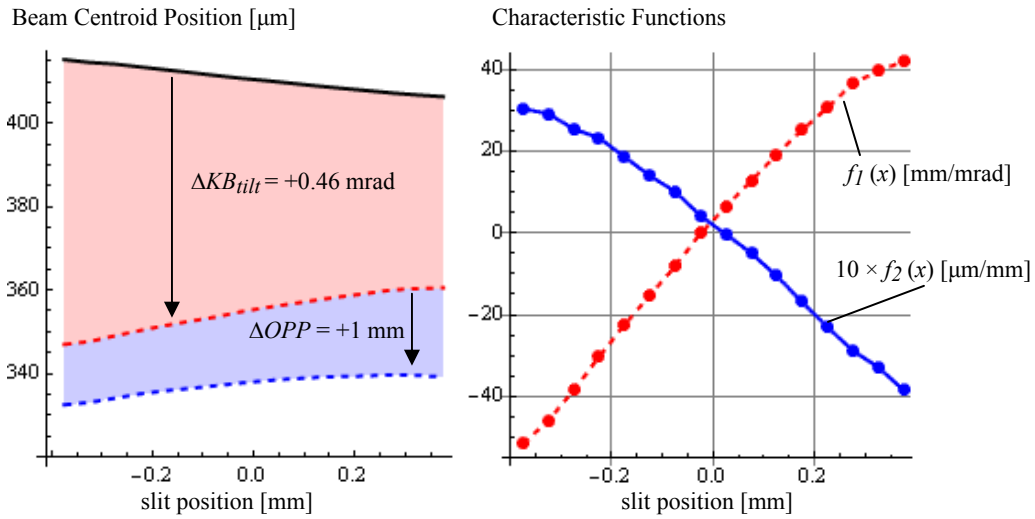

Figure 3. Measurement of the characteristic functions of the mirror tilt and observation plane position. (Left) The top solid graph is the initial beam centroid position on the microscope as a function of slit position, while the transition to the middle dashed line represents the response of this function to a +0.46 mrad change of the mirror tilt, and that of the bottom dashed line represents the additional response of the system to a 1 mm change of the observation plane position towards the mirror. (Right) The resulting characteristic function of the mirror tilt parameter (f_1) (dashed), and the measured characteristic function of the observation plane's longitudinal position displacement (f_2) (solid).

From the measured characteristic functions, and the initial alignment state, linear regression analysis was used to find the optimal parameter settings. Based on these measured characteristic functions, the optimal configuration of the system with respect to these parameters was obtained by increasing the mirror tilt by 88 μrad and retracting the observation plane from the mirror by a distance of 676 μm. The system alignment state following these changes is shown by the solid graph in Fig. 4. This is compared to the predicted optimal configuration represented by the dashed graph in Fig. 4, based on the characteristic functions. This actual optimum corresponds to an RMS ray error at focus of approximately RMS = 140 nm.

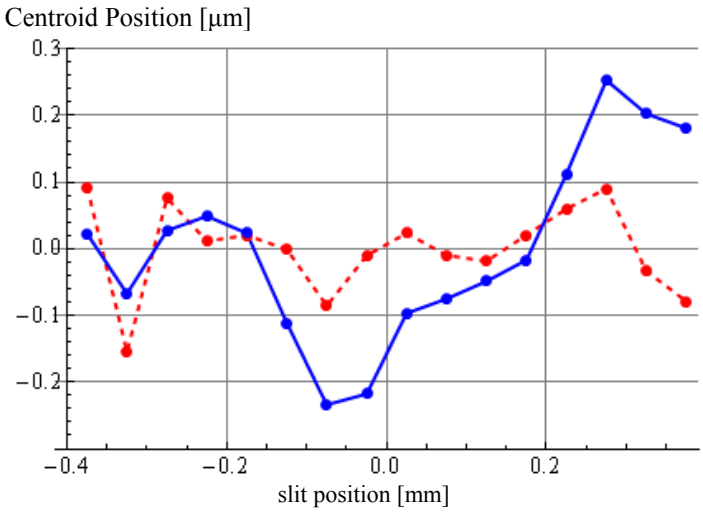

Figure 4. Beam translation about the mean *y*-position for the measured optimum (solid) and predicted optimum (dashed) configuration of mirror tilt, with RMS variations of 135 nm and 65 nm, respectively.

4.3 Rapid wavefront slope-error feedback from lateral shearing interferometry

We used lateral shearing interferometry[3] as feedback to perform the wavefront slope-error optimization by mirror bending. This interferometry method superimposes a diverging wavefront onto angularly-shifted versions of itself, created by diffraction through a linear grating. Interference is recorded on a CCD camera far downstream of focus where the beam size is large enough to make an accurate measurement of the interference fringes.

For a focused beam, wavefront slope errors decrease linearly with the distance from focus. Since shearing measures the wavefront slope in the plane of the CCD, transformation back to the mirror or another position requires scaling the measurement by a ratio of longitudinal distances from focus (e.g. z_{CCD}/z_{mirror}). For this reason, slopes measured with shearing appear smaller than expected (for a typical KB mirror), until they are scaled appropriately to the mirror position.

Taking advantage of the Talbot effect,[17] the far-field pattern is a self-image of the grating, with distortions caused by slope errors of the wavefront. Using a square wave grating with period d, placed close to the $z = d^2/\lambda$ Talbot distance from the focus, it can be shown that the intensity $I(x)$ appearing on the CCD can be approximated as a series of interfering, laterally-shifted diffracted orders

$$I(x) = \left| \sum_{n=-\infty}^{\infty} C_n \exp\left[i \frac{2\pi}{Md} nx \right] \exp\left[i\gamma\left(x - z \sin\theta_n\right)\right] \right|^2, \qquad (6)$$

where the C_n are the coefficients of the Fourier series expansion of the grating transmittance function (i.e. a binary square wave in this case), M is the magnification of the grating image, $\gamma(x)$ is the phase of the zeroth-order diffracted beam at the CCD, z is the distance from the grating to the CCD, and θ_n are the angles of the various diffracted orders, n, which obey the grating equation, $n\lambda = d\sin\theta_n$. In the case where $\gamma(x)$ is aberration free and cylindrically expanding, the

second exponent in Eq. (6) is constant and a magnified image of the grating forms on the CCD. Although the interference pattern potentially contains many overlapping orders, a simplification that is appropriate with small-magnitude aberrations with characteristic length scales larger than the shear distance retains only orders -1, 0 and 1. Here the phase difference that emerges is a combination of the -1 and 0 order difference, and the 0 and 1 order difference. Hence, it takes the form of a centered discrete derivative between orders separated by the shear distance. Ignoring the square shape of the fringes, the fundamental fringe periodicity takes the form

$$I(x) \approx A + B\cos\left(\frac{2\pi}{Md}x + \Delta\gamma(x)\right) \tag{7}$$

where A and B are constant coefficients. From the grating equation, we find that the first-order shear distance on the CCD plane is $z\lambda/d$. In Eq. 7, the discrete derivative is $\Delta\gamma(x) \equiv \gamma(x + s/2) - \gamma(x - s/2)$. The wavefront slope $W'(x)$ measured in the CCD plane, is given approximately by

$$W'(x) \approx \frac{d}{2\pi z}\Delta\gamma(x), \tag{8}$$

provided that the values of z and d are chosen such that $z\,\lambda/d << \gamma'(x) / \gamma''(x)$ (primes indicate differentiation) across the domain. This condition is readily found by inspection of the Taylor series representation of the finite difference function. The phase difference $\Delta\gamma(x)$ is recovered from the measured interferogram using the well-known Fourier transform method[21,22]. A third-order Butterworth filter was used in the Fourier domain to isolate the first order phase information from the rest.

4.4 At-wavelength optical optimization using a 1D lateral shearing interferometer

Our mirror slope-error measurements showed that the roll of the mirror (rotation about an axis along the beam-propagation direction) was initially, not well aligned. This alignment degree of freedom is difficult to accurately set when the mirror is transferred from the OML to the beamline. The roll error was clearly visible by eye in a shearing interferogram pattern of consistently tilted fringes. With an RMS slope error of 580 nrad in the sagittal tilt of the wavefront, roll was the dominant error before alignment. Figure 5 shows wavefront slope measurements before and after the roll-alignment. We estimate that the transverse mirror width illuminated by the beam and shown in the figures below is approximately 0.5 mm. Although the entire, 102-mm length of the mirror is illuminated during the shearing measurement, we discard 10% of the area from the each edge to match the normal operating conditions of the KB mirror produced by the beam-defining (movable-slit) aperture. After calibrating the system's response to small roll changes, we eliminated the sagittal tilt of the mirror in several steps.

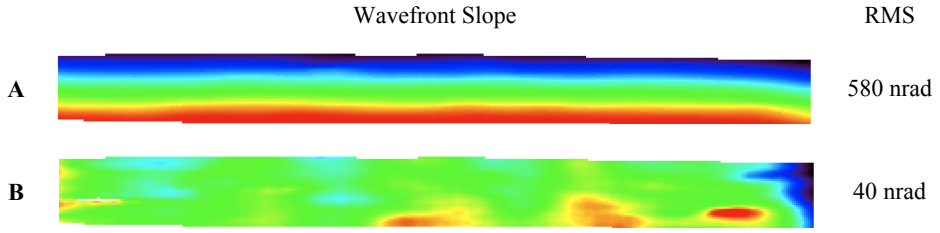

Figure 5. Comparison of wavefront slope before (A) and after (B) roll adjustment of test KB mirror using lateral shearing interferometer. The two slope measurements are shown in different color scales to emphasize the elimination of tilt in the sagittal direction. Slope values range from positive to negative through the red-to-black rainbow color scale. RMS slope values shown are measured in the plane of the CCD. The left side of the figure represents the upstream side of the mirror, farthest from focus. The beam measures approximately 0.5 mm in the transverse direction, and 80 mm along the mirror's length.

Following the roll-error correction, the tangential wavefront aberrations were minimized using MCF, in a manner similar to that described in Section 4.2, but with the shearing interferometry slope measurements as input. Here, the mirror was optimized with respect to the (two) bending couples on the upstream and downstream ends of the mirror. From the initial

state, we measured the characteristic functions of the wavefront slope error with respect to small adjustments of the two couples. These two characteristic functions are shown in Fig. 6. Both functions are normalized by their RMS values. They can be thought of as unit basis vectors in configuration space. We found that in this mirror holder, the bending sensitivity is close to 10× greater on the upstream side of the mirror, per micron of actuator motion. The graph on the right side shows us that the two functions are independent in the space spanned by the set of one-dimensional orthonormal polynomials over the measurement domain.

Optical aberrations are commonly classified by separating the contributions from orthonormal polynomials used to characterize the wavefront or slope-error measurement. Here, because measurements are given in wavefront slope, we associate zeroth and first-order polynomials, as functions of the lateral and longitudinal beam-focus position (i.e. tilt and defocus). We choose to optimize the wavefront aberrations globally, not at a particular, pre-specified (y, z) location, as might be necessary with a two-dimensional focusing system. The third and fourth order aberrations, commonly referred to as coma and spherical aberration in a rotationally symmetric optical system, are here identified with the second- and third-order polynomials in wavefront slope-error, respectively. Since the two characteristic functions are independent with respect to third and fourth order wavefront errors, a linear combination can be found, in principle, to eliminate them both from the final alignment of the optical system.

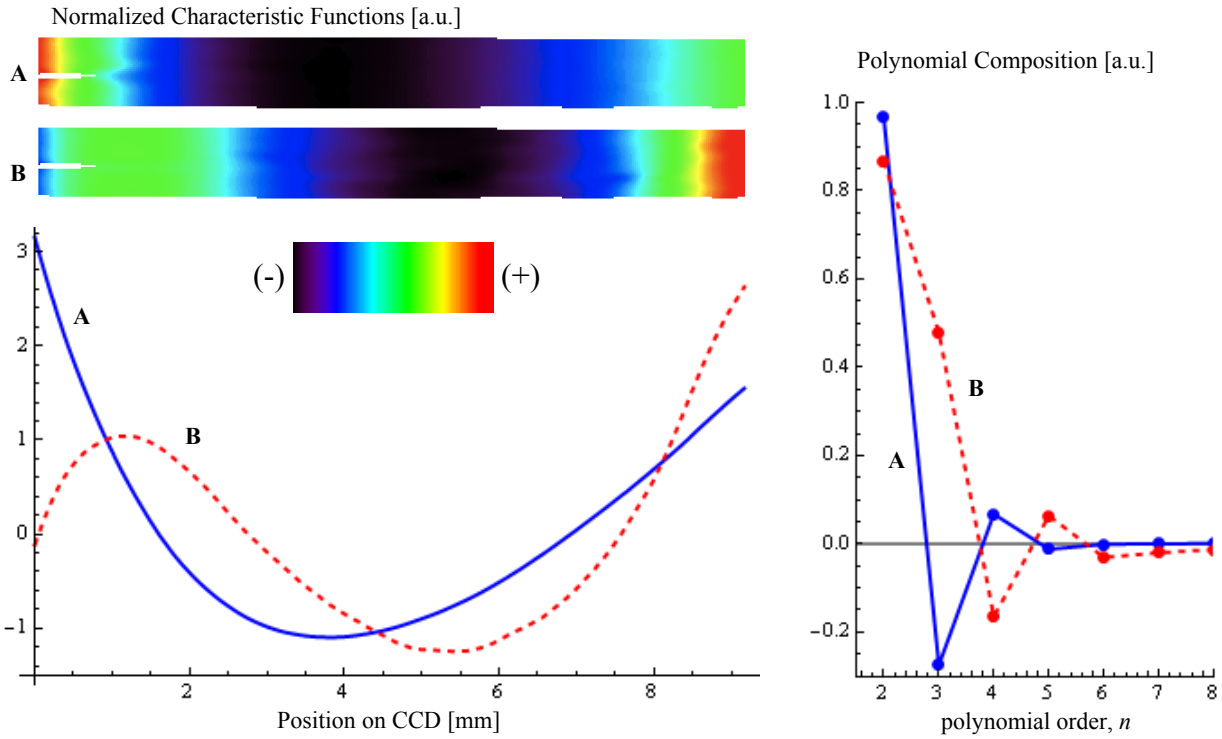

Figure 6. Characteristic functions of the two bend parameters. (Top Left) Normalized 2D characteristic functions for the upstream and downstream benders, labeled A and B, respectively. (Bottom Left) Normalized 1D characteristic functions for the upstream bender in solid, and the downstream bender as the dashed line, corresponding to the median values, taken along the sagittal direction, in the above images. (Right) The characteristic functions can be decomposed into sets of orthogonal polynomials, each of which represent a type of aberration contribution for each bender. The corresponding normalized coefficients of this decomposition are shown for the upstream bender characteristic function in solid, and for the downstream bender as the dashed line.

Following the MCF procedure, adjustment of the two bending couples produced a significant improvement in the RMS wavefront slope error, from 64 nrad to 24 nrad, as shown in Fig. 7. Figures 7A and B illustrate the initial and final states of the measured wavefront slope error. The optimization was performed in three steps. Figure 8 shows the polynomial coefficients of the wavefront slope errors for these two configurations—we use a one-dimensional basis set that is

orthonormal on the CCD camera's measurement domain. Most of the improvement came from the reduction of third- and fourth-order wavefront errors (coefficients 2 and 3 in the slope), as expected. Higher-ordered aberrations were less affected by the bending and may arise from shorter-length-scale imperfections in the mirror surface.

Seeking to further reduce aberrations, we also investigated the characteristic functions of the mirror tilt (i.e. changing the glancing angle). Interestingly, we found that this characteristic function strongly overlapped the shape of the upstream bending couple's characteristic function, when wavefront tilt and defocus were removed. This degeneracy between two free parameters in the alignment frustrates the simple optimization by linear regression, and for this reason, we did not perform tilt optimization at the same time as the bending (i.e. as a three-parameter optimization).

In a more general context, this observation has a different interpretation. If the mirror tilt is included with the bending couples as a third free parameter in the optimization, then the observe that the elimination of wavefront aberrations can occur for one trivial solution to the optimization process: that is, the complete unbending (i.e. flattening) of the mirror with respect to the beam. In such a hypothetical case, the high-quality spherical wavefront from the slit is the only source of wavefront curvature (albeit a diverging curvature) and the higher ordered aberrations would be eliminated. This is clearly not the zero-slope-error solution we seek.

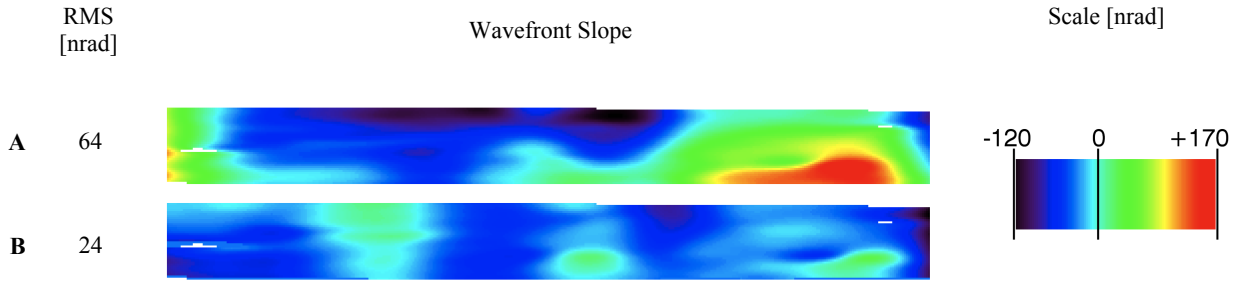

Figure 7. Wavefront slope before (A) and after (B) optimization using the lateral interferometry method combined with the method of characteristic functions. Red indicates higher values of slope error, while black indicates lower values, in an absolute scale. Intermediate values are depicted according to a rainbow sequence. Note: RMS wavefront slope-error values are given in the plane of the CCD. Mirror slope values are approximately 6 times larger.

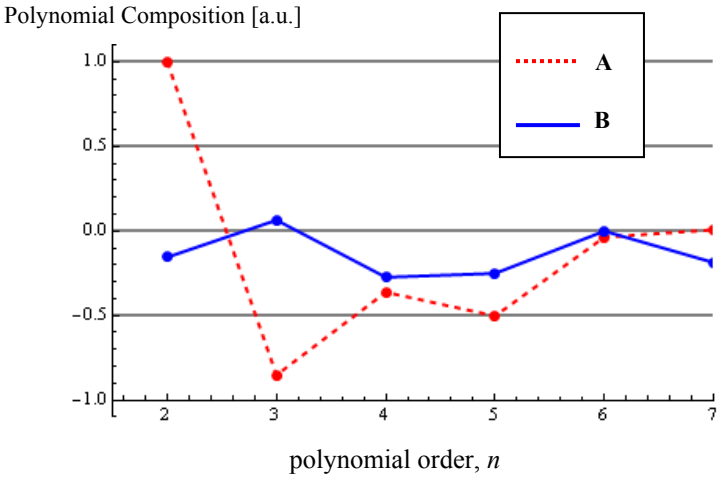

Figure 8. Orthonormal polynomial coefficients of the wavefront slope aberration for the initial configuration (A) and the final optimized configurations (B).

4.5 Measuring the beam waist

Knife-edge testing serves as unambiguous confirmation of the focused beam size following wavefront optimization. In the absence of aberrations, diffraction dictates the minimum size of the focused beam. For a uniformly illuminated, one-dimensional focusing system, an approximation to the diffraction limited focused spot size (FWHM) is $\Delta l \approx \lambda / 2\,NA$, which in our case is 135 nm. Using the simpler form of the Foucault knife-edge test, as described in Section 3.3, we measured a beam FWHM of 154 ± 10 nm at focus. Measurements were made using the CCD camera, summing the signal across the projected pupil domain, after background subtraction.

The results of the knife-edge tests are summarized in Fig. 9, with the beam width at focus is shown on the left, and the sequence of FWHM beam widths through focus are shown at right. The beam profile strongly correlates with a Gaussian profile. The R^2 value of the fit of flux vs. knife position to the *error function* is 0.999 at focus. For all knife-edge measurements, the R^2 value for fits to the error function are greater than 0.995. Based on this high correlation, FWHM beam widths reported are deduced from derivatives of the best fitting error functions, rather than from interpolation, which can be inaccurate due to point-to-point beam intensity variations.

Recording the knife-edge signal with the CCD camera provides additional information about the beam focusing. Within the full aperture projected onto the detector, we can selectively analyze arbitrary solid angles that exclude the upstream and downstream edges of the mirror (e.g. by summing the signal from specific sub-domains of the data). This allows us to probe the relationship between the beam waist and the NA, or to effectively eliminate the influence of poorly aligned mirror sections near the edges of the domain. The data gathered from these tests can guide the selection of an optimal entrance slit width to produce the tightest beam focusing.

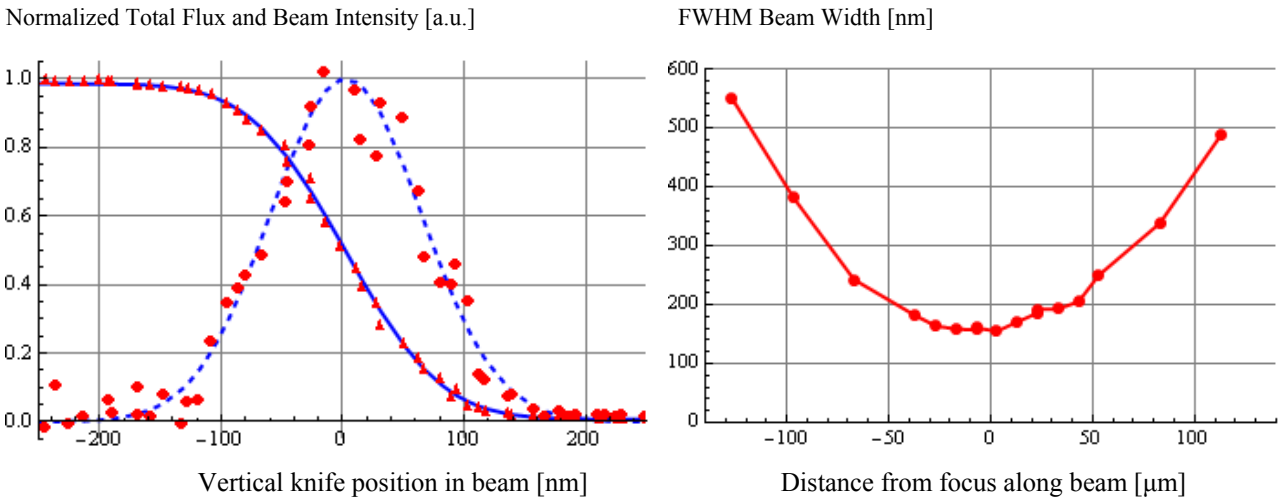

Figure 9. (Left) Measured flux (triangles) vs. knife-edge position and fitted error function (solid line). Circles indicate the finite forward difference of the flux data and the dashed line is the derivative of the fitted error function. Both the flux and profile are normalized to unity for display. (Right) FWHM beam width as a function of displacement along the propagation direction.

5. COMPARISON OF IN SITU AND EX-SITU METROLOGY

Studying the correspondence of *in situ* at-wavelength testing with *ex situ* visible-light testing is a significant goal of this project, and an important area for the development of high-quality x-ray optics. Such comparison can be particularly challenging when the absence of fiducial marks on the mirror surface leads to uncertainty in the sagittal x-ray beam position during measurement.

Slope-errors are not an intrinsic characteristic of a propagating spherical or cylindrical wavefront. Unlike small wavefront errors, which maintain their relative absolute magnitudes as waves propagate, slope errors decrease in proportion to their distance from focus. Therefore, taking into account the plane of measurement (the CCD in the shearing interferometry, for example) is an essential part of the accurate reconstruction of the wavefront properties at a

different location, such as the surface of the mirror. Furthermore, since glancing incidence focusing mirrors vary in their distance from focus along the propagation direction, a variable scaling factor must be applied in the point-by-point transformation from measurement plane to mirror surface. In the present case, this variation is significant, with the mirror stretching from 70 to 170 mm from focus along its length. It is well known that for glancing-incidence focusing mirrors, slope-errors in the regions farther from focus will cause more significant ray errors than equivalent errors closer to focus, simply by the difference in the propagation distances.

The transformation from wavefront slope error to mirror-surface slope error was carried out in the following way, according to Fig. 10. We first used Zemax™ to calculate the mapping between each point A, with coordinate u, on the test mirror and the point v on the CCD camera, connected by the ideal light ray, depicted by the dashed arrow. The result is the function $v = f(u)$, reported previously for this particular system.[5] Next, we assumed that the slope of the wavefront error was sufficiently small such that for every point u on the mirror, the deviation δv due to the ray error was negligible, i.e. much smaller than the width of pixels at the plane of the CCD. In this assumption, each CCD pixel is uniquely associated with a point on the mirror, regardless of the (small) ray errors. This requirement sets a maximum ray error for a half-pixel ray displacement on a CCD with 24 μm pixels at 1.8 m distance at $\delta\alpha < 7$ μrad. This condition is easily met for the points on the mirror within 40 mm of the center. Previous OML measurements[2] give an estimate of 0.8 ± 0.2 μrad RMS ray slope error. The lateral shearing interferometer measures a wavefront slope error or ray slope error $\delta\beta$ at the CCD camera plane, a distance z downstream of the focus point B; the ideal wavefront is shown as the dotted line passing through C. The slope error $\delta\beta$ is the angle that the actual wavefront makes with the hypothetical, ideal wavefront with radius of curvature z, at the point C. By the law of sines,

$$\frac{\sin\delta\alpha}{z} = \frac{\sin\delta\beta}{r'-u}, \tag{11}$$

Finally, a ray error $\delta\alpha$ from the point A on the mirror is caused by a mirror slope error δs_A at A of one half $\delta\alpha$, or

$$\delta s_A = \frac{1}{2}\frac{z}{r'-u}\delta\beta_C, \tag{12}$$

where $\delta\beta_C$ is the wavefront slope error measured at the point C and the angles are assumed small. These slope transformations enable us to deduce the mirror slope error from wavefront slope error measured with lateral shearing interferometry.

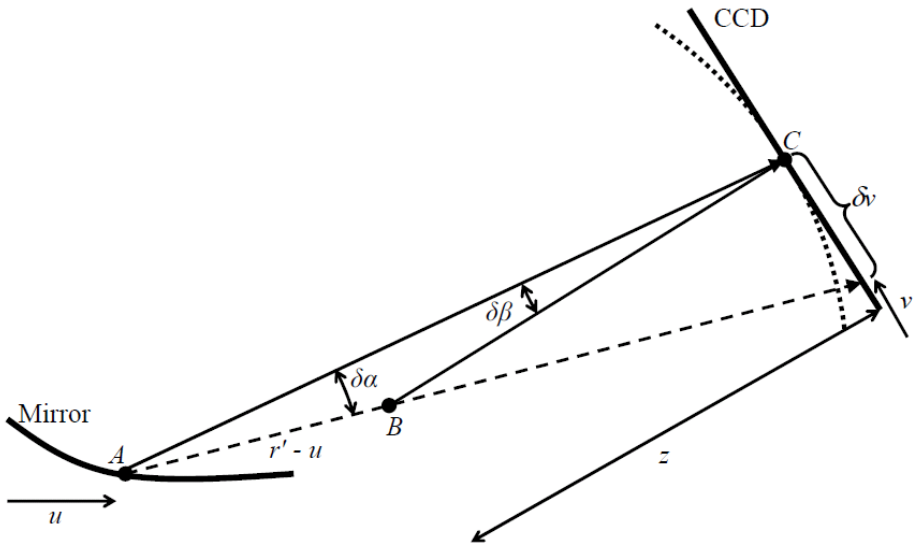

Figure 10. Geometry of (exaggerated) wavefront/ray aberrations in the 1D focusing system. The length of segment AB is shown as $r' - u$ because the angle between AB and the u-axis is merely 8 mrad, which is neglected for simplicity.

Figure 11 summarizes the comparison between slope error measured at-wavelength with the lateral shearing interferometer and slope error measured in the OML with the LTP-II++. The mirror slope error measured in the OML is shown in circles and the mirror slope error measured by lateral shearing is marked with triangles. Both measurements were taken after the mirror was optimized. The slope error profile shown from the lateral shearing interferometer is the sagittal average across the analyzed portion of the pupil (the middle 80% of the mirror). The RMS slope errors measured in each way are 0.24 ± 0.1 μrad (OML), 0.27 ± 0.05 μrad (shearing). The uncertainty in the shearing measurement is estimated based on the repeatability.

Recently, mirror optimization in the OML has been improved by allowing the r' conjugate distance the glancing angle θ to vary in order to balance residual slope errors.[1] In this work, after the test mirror was optimized at-wavelength, and re-measured with visible-light in the OML, we implemented a fitting routine that allows the assumed conjugate and incidence-angle values to vary slightly, within 1% of the design values: r = 1650 mm, r' = 120 mm and θ = 8 mrad, in the least squares linear regression procedure. This allowed us to take into account inaccuracies in the placement and alignment of the mirror at the beamline endstation, which change these values. By implementing this procedure, the new best-fit mirror profile was r = 1650.96 mm, r' = 119.39 mm and θ = 8.063 mrad. Subtracting this ellipse from the measured slope data resulted in the slope error profile found in Fig. 11.

At this point, the systematic errors of the lateral shearing interferometer have not been fully characterized. However, based on repeated sequential measurements of the wavefront slope (i.e. with the grating translated in plane between measurements), the measurement-to-measurement repeatability of the wavefront slope error is on the level of 5 nrad, measured at the CCD position. This corresponds to measurement-to-measurement repeatability of approximately 0.05 μrad in measured mirror slope error. The agreement between the OML and the shearing measurements of the mirror slope error is a noticeable improvement over the previous work.[5] This is due to both a better compensation of the defining parameters $\{r, r', \theta\}$ in the OML measurements, and a more accurate transformation of measured at-wavelength wavefront slope error to mirror slope error.

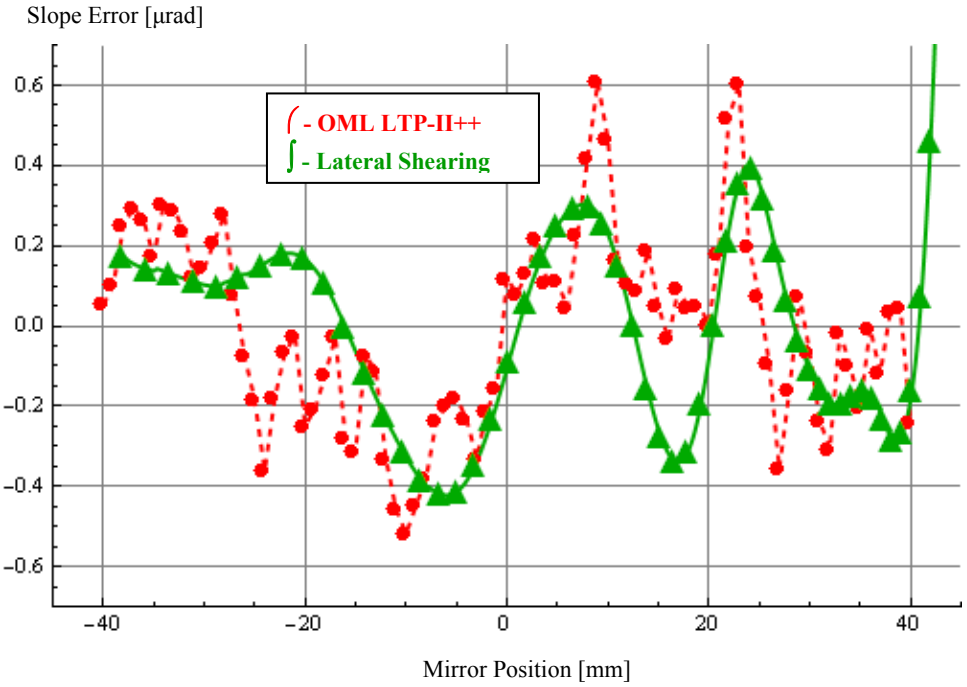

Figure 11. Comparison of *in situ* and *ex situ* metrology: mirror slope error measured *ex situ*, in the OML (solid circles), and measured *in situ* with the lateral shearing interferometer (crosses). Positive values of the mirror position are *downstream*, in the direction of beam propagation.

CONCLUSIONS

Reliable diffraction-limited soft x-ray nano-focusing requires the development of practical techniques that can accurately and routinely sense and correct small wavefront and slope errors. At the ALS, established *ex situ* optical metrology methods are being matched with emerging *in situ* at-wavelength methods capable of sensing sub-100-nrad slope errors and nanometer-sized focal spots. In conjunction, these techniques are being developed with minimal hardware requirements and maximum transferability.

In this work, we have developed a comprehensive procedure for the alignment and testing of a single bendable Kirkpatrik-Baez mirror, for focusing of soft x-rays in one dimension. Using well established and state-of-the-art techniques the mirror was pre-shaped in the OML using the LTP-II++. The mirror was then transferred to an ALS beamline, where it underwent a coarse alignment of the mirror tilt and focal plane. Then, using a 1D grating-based lateral shearing interferometer, the focusing soft x-ray wavefront was optimized in three steps to eliminate residual aberrations. The optimization used the MCF procedure based on the measured wavefront dependencies from each alignment degree of freedom. Direct, knife-edge measurements of the beam waist showed a 154 ± 10-nm spot size, 14% larger than the ($\lambda/2NA$) diffraction limited value. Finally, wavefront slope errors measured with lateral shearing interferometry and transformed onto the mirror surface showed quantitative agreement between the RMS slope errors, 0.24 vs. 0.27 μrad (OML vs. shearing), and similar prominent features in the slope profile.

Following this 1D demonstration, we will apply similar techniques to a 2D (two mirror) KB focusing system in the same experimental test chamber. Ongoing investigations of the knife-edge and scanning slit techniques provide additional data for comparison and learning. To conclude, the synthesis of *in-situ* and *ex-situ* metrologies provides a firm foothold for the next steps in x-ray at-wavelength metrology and nano-focusing at current and future high-brightness short-wavelength light sources.

ACKNOWLEDGEMENT

The Advanced Light Source is supported by the Director, Office of Science, Office of Basic Energy Sciences, Material Science Division, of the U.S. Department of Energy under Contract No. DE-AC02-05CH11231 at Lawrence Berkeley National Laboratory. This document was prepared as an account of work sponsored by the United States Government. While this document is believed to contain correct information, neither the United States Government nor any agency thereof, nor The Regents of the University of California, nor any of their employees, makes any warranty, express or implied, or assumes any legal responsibility for the accuracy, completeness, or usefulness of any information, apparatus, product, or process disclosed, or represents that its use would not infringe privately owned rights. Reference herein to any specific commercial product, process, or service by its trade name, trademark, manufacturer, or otherwise, does not necessarily constitute or imply its endorsement, recommendation, or favoring by the United States Government or any agency thereof, or The Regents of the University of California. The views and opinions of authors expressed herein do not necessarily state or reflect those of the United States Government or any agency thereof or The Regents of the University of California.

REFERENCES

[1] Yuan, S., Yashchuk, V. V., Goldberg, K. A., Celestre, R., McKinney, W. R., Morrison, G. Y., Warwick, T., and Padmore, H. A., "Development of in situ, at-wavelength metrology for soft X-ray nano-focusing," Nucl. Instrum. Meth. A, 649, 160-162 (2011).

[2] Yuan, S., Goldberg, K. A., Yashchuk, V. V., Celestre, R., Mochi, I., MacDougall, J., Morrison, G. Y., Smith, B. V., Domning, E. E., McKinney, W. R., and Warwick, T., "At-wavelength optical metrology development at the ALS," Proc. SPIE, 7801, 78010D (2010).

[3] Naulleau, P. P., Goldberg, K. A., and Bokor, J., "Extreme ultraviolet carrier-frequency shearing interferometry of a lithographic four-mirror optical system " J. Vac. Sci. Technol. B, 18(6), 2939-2943 (2000).

[4] Stewart, D., "A Platform with Six Degrees of Freedom," Proc. Institution of Mechanical Engineers (UK), 180 Pt. 1(15), (1965).

[5] Yuan, S., Goldberg, K. A., Yashchuk, V. V., Celestre, R., McKinney, W. R., Morrison, G., Macdougall, J., Mochi, I., and Warwick, T., "Cross-check of ex-situ and in-situ metrology of a bendable temperature stabilized KB mirror," Nucl. Instrum. Meth. A, 635(2011), S58–S63 (2010).

[6] Yuan, S., Church, M., Yashchuk, V. V., Goldberg, K. A., Celestre, R. S., McKinney, W. R., Kirschman, J., Morrison, G., Noll, T., Warwick, T., and Padmore, H. A., "Elliptically Bent X-Ray Mirrors with Active Temperature Stabilization," X-Ray Opt. Instrum., 2010, 784732 (2010).
[7] Yuan, S., "Surface Slope Metrology on Deformable Soft X-ray Mirrors," Lawrence Berkeley National Laboratory(LBNL-2645E), (2010).
[8] Howells, M. R., Cambie, D., Duarte, R. M., Irick, S., MacDowell, A. A., Padmore, H. A., Renner, T. R., Rah, S., and Sandler, R., "Theory and Practice of Elliptically Bent X-ray Mirrors," Opt. Eng., 39(10), 2748 – 2762 (2000).
[9] McKinney, W. R., Irick, S. C., Kirschman, J. L., MacDowell, A. A., Warwick, T., and Yashchuk, V. V., "New procedures for the adjustment of elliptically bent mirrors with the long trace profiler," Proc. SPIE, 6704, 67040G (2007).
[10] McKinney, W. R., Kirschman, J. L., MacDowell, A. A., Warwick, T., and Yashchuk, V. V., "Optimal tuning and calibration of bendable mirrors with slope-measuring profilers," Opt. Eng., 48(8), (2009).
[11] Hignette, O., Freund, A. K., and Chinchio, E., "Incoherent x-ray mirror surface metrology," Proc. SPIE, 3152, 188-199 (1997).
[12] Naulleau, P. P., Batson, P., Denham, P., Richardson, D., and Underwood, J., "An in situ scanning-slit alignment system for Kirkpatrick–Baez optics," Opt. Commun., 212, 225–233 (2002).
[13] Mercère, P., Zeitoun, P., Idir, M., Pape, S. L., Douillet, D., Levecq, X., Dovillaire, G., Bucourt, S., Kenneth A. Goldberg, Naulleau, P. P., and Rekawa, S., "Hartmann wave-front measurement at 13.4 nm with λEUV/120 accuracy," Opt. Lett., 28(17), 1534-1536 (2003).
[14] Gaviola, E., "On the quantitative use of the foucault knife-edge test," J. Opt. Soc. Am., 26, 163-169 (1936).
[15] Vandenberg, D. E., Humbel, W. D., and Werthelmer, A., "Quantitative evaluation of optical surfaces by means of an improved Foucault test approach," Opt. Eng., 32(8), 1951-1954 (1993).
[16] Cheng, H. B., Yam, Y., and Tong, H., "A quantitative knife-edge testing method for local deformation evaluation in optical aspheric fabrication," Proc. of the 3rd Annual IEEE Conference on Automation Science and Engineering, 818-822 (2007).
[17] Malacara, D., [Optical Shop Testing] John Wiley & Sons, Hoboken(2007).
[18] Kirschman, J. L., Domning, E. E., McKinney, W. R., Morrison, G. Y., Smith, B. V., and Yashchuk, V. V., "Performance of the upgraded LTP-II at the ALS Optical Metrology Laboratory," Proc. SPIE, 7077, 70770A (2008).
[19] McKinney, W. R., Anders, M., Barber, S. K., Domning, E. E., Lou, Y., Morrison, G. Y., Salmassi, F., Smith, B. V., and Yashchuk, V. V., "Studies in optimal configuration of the LTP," Proc. SPIE, 7801, 780106 (2010).
[20] Yashchuk, V. V., "Sub-microradian Surface Slope Metrology with the ALS Developmental Long Trace Profiler," Nucl. Instrum. Meth. A, 616(2-3), 212-223 (2009).
[21] Takeda, M., Ina, H., and Kobayashi, S., "Fourier-transform method of fringe-pattern analysis for computer-based topography and interferometry," J. Opt. Soc. Am., 72(1), 156-160 (1981).
[22] Bone, D. J., Bachor, H.-A., and Sandeman, R. J., " Applied Optics, 25 (10), "Fringe-pattern analysis using a 2-D Fourier transform," Appl. Opt., 25(10), 1653-1660 (1986).